

Full paper

Electroactive properties of electrospun silk fibroin for energy harvesting applications

Vitor Sencadas^{a,b,c,*}, Christopher Garvey^d, Stephen Mudie^e, Jacob J.K. Kirkensgaard^f,
Gwenaël Gouadec^g, Samuel Hauser^a

^a School of Mechanical, Materials, Mechatronic and Biomedical Engineering, University of Wollongong, Wollongong, NSW, 2522, Australia

^b ARC Center of Excellence for Electromaterials Science, University of Wollongong, 2522, NSW, Australia

^c Illawarra Health and Medical Research Institute, University of Wollongong, NSW, 2522, Australia

^d Australian Nuclear Science and Technology Organization (ANSTO), Locked Bag 2001, Kirrawee DC, NSW, 2232, Australia

^e Australian Synchrotron, ANSTO, 800 Blackburn Rd, Clayton, 3168, Australia

^f Department of Food Science, University of Copenhagen, Denmark

^g Sorbonne Université, CNRS, Laboratoire MONARIS, c49, F75252, Paris, France

ARTICLE INFO

Keywords:

Silk fibroin
Natural proteins
Piezoelectricity
Energy harvester
E-skin

ABSTRACT

Silk fibroin (SF) is a sustainable material explored with success in the textile and biomedical industries. This protein has outstanding mechanical and electrical properties that could be used for advanced technological applications. In this work, silk fibroin fibrous membranes were processed by electrospinning, with conditions obtained through orthogonal experimental design. Due to their high-water affinity, the membranes were stabilized against aqueous environments by exposure to methanol (MeOH) in vapor phase. Individual SF fibres present an apparent piezoelectric constant (d_{33}) of 38 ± 2 pm/V for the as-spun ones and 28 ± 3 pm/V for those submitted to MeOH in vapor phase, a piezoelectric voltage coefficient (g_{33}) of 1.05 and 0.53 Vm.N⁻¹, respectively, a mechano-sensibility of 0.15 V kPa⁻¹, an energy storage capacity of 85 μJ, and an efficiency up to 21%. When the SF is submitted to MeOH in vapor phase, no effect was observed in the protein secondary structures. This work represents a new insight into the origin of the piezoelectric properties of SF and opens new opportunities for applications in microelectronics engineering for self-powered epidermal electronics, implantable medical devices, and personalized health care systems.

1. Introduction

Silk obtained from the formation of the cocoon during the larval stage of the *Bombyx mori* moth has been used in the textile industry for more than 5000 years [1–3]. Due to a combination of outstanding properties [1], this widely available material has since found a wide range of applications, e.g. air cleaning filters [4], drug delivery [5], and tissue engineering [6].

Silkworm cocoons are made from two main proteins: fibroin and sericin [7]. Silk fibroin has attracted technological and scientific interest, due to its outstanding mechanical, electrical and biological properties whereas sericin, a water-soluble and glue-like protein representing 30% of the cocoon material, is mainly responsible for holding the fibrous fibroin [6,7]. Sericin is commonly removed by various techniques, like high pressure and high temperature methods, enzyme extraction, or acid or alkaline solutions [8], a process known by degumming [7]. After sericin removal, the silk fibroin (SF) fibers are

submitted to a water-based dissolution process, being readily available for further manufacture into different materials [5,7]. The resulting silk fibroin form is a semi-crystalline material [1,9], where ordered lamellar regions are tied by an amorphous matrix.

Silk fibroin is a copolymer of heavy chain (molecular weight approximately 350 kDa) and light chain (26 kDa) proteins, linked together by disulfide bridges [10–12]. In addition, P25 glycoprotein (36 kDa) associates with the disulphide-linked chains by noncovalent interactions. While the heavy chain is predominantly made of alternating hydrophobic oligopeptides, the light chain is mainly hydrophilic and contains a high concentration of glutamic and aspartic acid residues [7,10].

At least five different silk structures have been identified, with specific molecular packing and individual amino acid sequences, and hydrogen bonding between the polymer chains contributing to the overall mechanical performance [1–3]. The metastable coil-coil structure is made from hydrophobic polar groups and adopts a right-handed

* Corresponding author. School of Mechanical, Materials, Mechatronic and Biomedical Engineering, University of Wollongong, Wollongong, NSW, 2522, Australia.
E-mail address: victors@uow.edu.au (V. Sencadas).

helix motif with 3.5 amino acids per turn (α -helix), also designated silk I. Silk II is organized in extended and trans-planar β -sheets parallel to the fiber axis, with alternate amino acids side chains projected to opposite sides of the sheet. Turns and bends are made of β -sheet strands of uniform length along which the polymer chain makes a U-turn, and the sheets stack face to face (the beta strands direction is perpendicular to the fiber axis). The triple helix collagen configuration can also be found in silk structure with a left-handed helix (3 amino acids per turn). The last conformation is the polyglycine II, where the amino acids adopt a right-handed helix motif with three amino acids per turn [1,10,13].

Silk fibroin presents a crystalline dimorphism, where the silk II crystals have a monoclinic unit cell [9,14], while silk I crystallizes in an orthorhombic one [14]. The lack of center of symmetry in both crystalline units suggests that silk fibroin is piezoelectric, independently of the crystalline polymorphism present in the protein.

Piezoelectricity is found in non-centro symmetric materials when a mechanical stress results in an electrical output (direct effect), or when applying a voltage makes the sample either expand or contract (inverse piezoelectric effect) [15]. Piezoelectricity can be found in ceramics like barium titanate (BaTiO_3) [16], lead zirconate titanate (PZT) [17,18], quartz or Rochelle salt [19,20], or synthetic polymers like poly(vinylidene fluoride) (PVDF) [21–23] and (vinylidene fluoride) (VDF) copolymers [24,25]. Recently, it was reported that some biopolymers show intrinsic shear piezoelectricity, where the electrical output is a result of a shear deformation, e. g. collagen [26], gelatin [27], wood, cellulose, keratin [20] or poly(lactic acid) (PLA) [28].

The electroactive properties of silk fibroin were reported by Harvey in 1939 [29], when he found that rubbing steel balls with silk fragments generated charges, and this phenomenon was first attributed to triboelectricity or piezoelectricity. The first quantitative measurements of silk piezoelectricity were made by Fukada [9] and reported a

piezoelectric response of $\approx 1 \text{ pC.N}^{-1}$, similar to the piezoelectric constant of quartz crystal ($\approx 2 \text{ pC.N}^{-1}$) [19,26].

More recently, Yucel et al. [10] prepared silk fibroin films and characterized their piezoelectric properties. It was found that oriented silk II presented a piezoelectric constant of 1.5 pC.N^{-1} , and inducing beta-sheet formation by immersion of the films in methanol did not result in a significant enhancement of its piezoelectricity, despite the increase of sample crystallinity. The samples prepared by Fukada [9] and Yucel et al. [10] were used as processed, without further electrical poling, and this could be the main reason for the poor electroactive properties reported.

In this work, we fully characterize the origin of silk piezoelectric properties. Silk fibroin processed by electrospinning has a high degree of polymer chain orientation along the fiber axis and is readily electrically poled. The electroactive properties of the protein were assessed by piezo-force microscopy (PFM) and correlated with its crystalline structure. A simple and cost-effective device was fabricated to demonstrate the remarkable electroactive properties of this protein for energy scavenging and harvesting. The wearable nano-harvester device shows potential to be used in real-time monitoring of human physiological signals. Moreover, this work opens up new opportunities to explore silk fibroin as a self-powered material for biomedical and tissue engineering applications.

2. Results and discussion

2.1. Morphology and structural characterization

Electrospinning processing parameters e.g. applied electric field, viscosity, feed rate or even the collection procedure, deeply influence fiber morphology [30,31]. The most common processing parameters

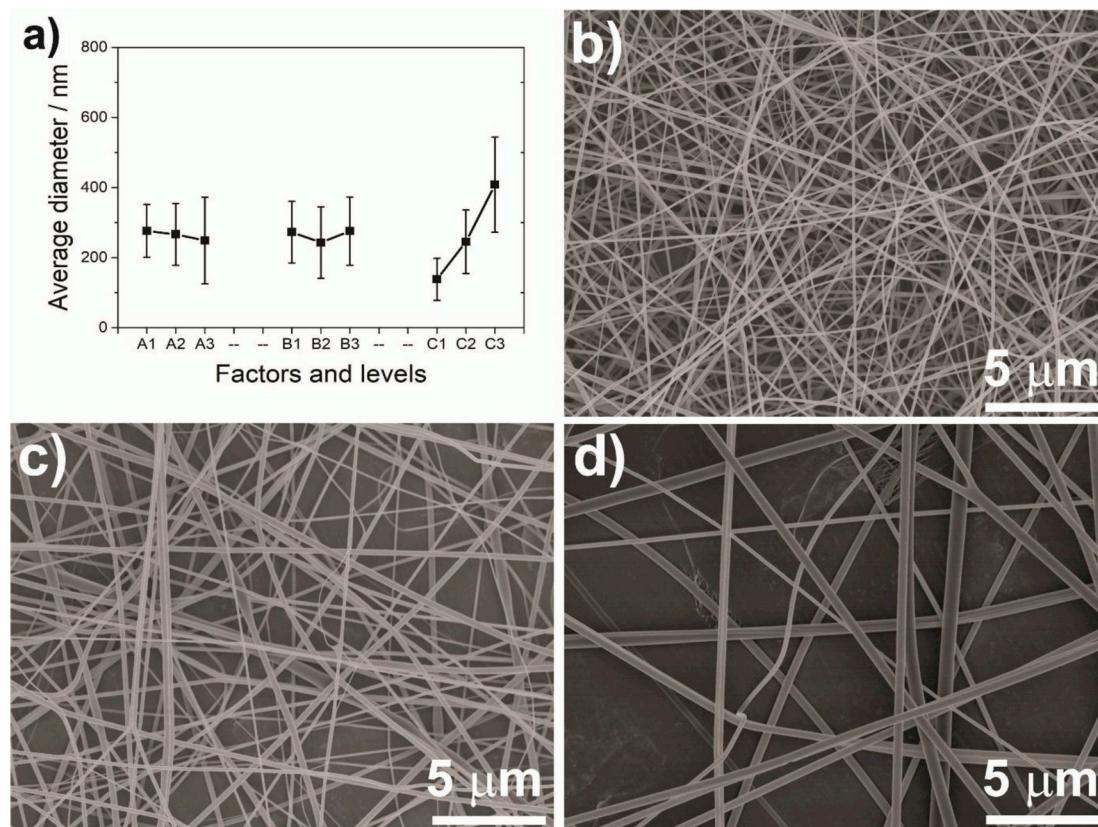


Fig. 1. a) Dependence of the average fiber diameter on the processing factors and levels used in the orthogonal design of electrospun silk fibroin membranes. SEM images are shown for conditions C1, C2 and C3 ($E = 0.75 \text{ kV.cm}^{-1}$, feed rate 0.2 mL.h^{-1} and a polymer concentration of: b) $40 \mu\text{g mL}^{-1}$ (4 wt%); c) $50 \mu\text{g mL}^{-1}$ (5 wt%) and d) $70 \mu\text{g mL}^{-1}$ (7 wt%).

with impact in processing stability and fiber geometry are the applied electric field (A), feed rate (B) and polymer concentration (C, Tables S1, S2 and S3). The experimental design used in this work showed that the average fiber diameter is influenced mostly by the polymer concentration (Fig. 1, Table S2 and Table S3).

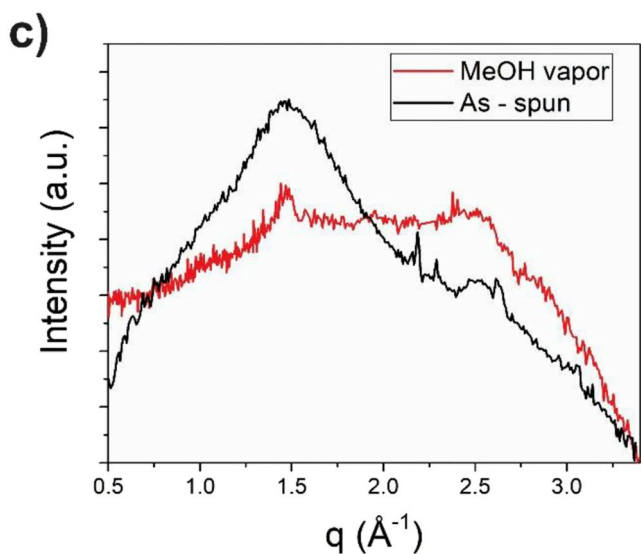
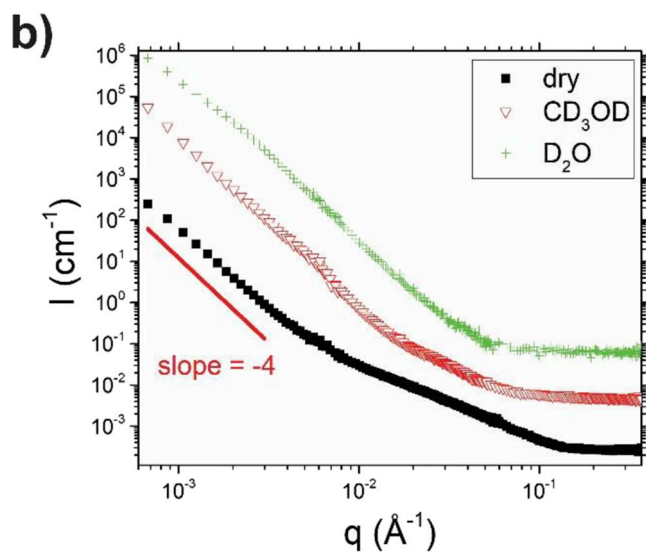
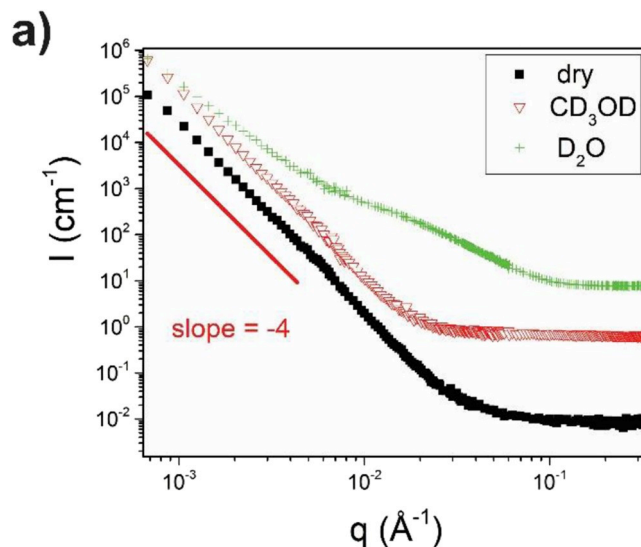
For polymer concentrations below $40 \mu\text{g mL}^{-1}$, a mixture of polymer fibers and beads was detected due to the low polymer entanglement: As the jet travels between the needle tip and the grounded collector, it is indeed stretched (due to the applied electrical field) but a minimum of polymer chain entanglement is necessary to maintain its stability and promote a continuous process [30]. For concentrations higher than $70 \mu\text{g mL}^{-1}$, the protein started to solidify and clogged the tip of the needle, independently of the applied electrical field or feed rate. After finding the window with the optimal processing conditions (Table S3), all the remaining samples presented a smooth and bead free morphology (Fig. 1).

After understanding the influence of the different electrospinning parameters on the fiber morphology, only one sample, with the conditions that lead to the thinnest fiber average diameter ($79 \pm 76 \text{ nm}$; condition C1 in Fig. 1a) was chosen to perform the characterization and assess the energy harvesting performance.

After processing, the electrospun mat was stabilized against the aqueous environment by placing the fibrous mats in a vacuum chamber saturated with methanol (MeOH) during 3 h. After exposure to MeOH, all the membranes showed excellent robustness against bending, stretching or compression, which is a useful property where the mechanical features are a key requirement, e.g. for applications as wearable sensors or energy scavenging and harvesting devices.

Small-angle neutron scattering (SANS) measurements were undertaken to understand the interaction of the fibre mats with methanol and water solvents. For this purpose, both the as-spun and MeOH-vapor treated mats were observed in air (“dry”) or immersed in deuterated methanol (CD_3OD) and water (D_2O). Except for the as-spun sample in D_2O , which became translucent, all samples remained opaque in the two solvents. Because of the difficulty of normalizing SANS curves to the volume fraction of fibroin in the neutron beam, absolute scaling of the scattering cross sections has been ignored in Fig. 2, and a simple comparison of the curves' shape is made. The dry as-spun fibers show two features plus a broad background signal parallel to the q -axis. This constant q -independent signal is due to the fibroin polymer and is dominated by the incoherent cross-section of hydrogen [32]. It is found in all samples and obscures details of the smallest structures in the SANS pattern. In the low- q limit, the -4.00 ± 0.05 slope on the $\log(I(q))$ versus $\log q$ scale, or Porod behavior, is typical of objects with a clear flat/zero-curvature interfacial boundary on the corresponding length-scales (~ 10 – 100 nm) [33]. The onset of the -4 slope is found in different q -regimes for different samples and is a direct indication of length-scales for the consolidation of polymer. The macroscopically translucent as-spun sample immersed in D_2O exhibits a $-3 \log I(q)/\log q$ slope which is indicative of a stronger interaction with water and the least consolidation of the fibroin structure.

In air, the MeOH treated fibers exhibit an intermediate region between $-0.06 < q < 0.11 \text{ \AA}^{-1}$. We suggest that the treatment of the initially silk I with MeOH vapor leads to swelling and refolding of the aligned fibroin molecules, leaving some free volume which is responsible for this internal structure within the fiber. With immersion in CD_3OD and D_2O , this region of the SANS curves incrementally disappears until only the abovementioned Porod behavior and incoherent background remain. The hydrophobic nature of the structures and internal surfaces formed by the prevalent silk II folding [1], would incur an energetic cost of hydration and a short range attractive van der Waals interaction, which would favor further consolidation of the structure [34]. These general observations would provide a physically reasonable rationalization of the loss of the intermediate- q SANS behavior of the MeOH treated fibers from the dry to the fibers in methanol and water, as the fibers densify and lose internal porosity.



(caption on next page)

Fig. 2. SANS curves for membranes observed either in air (dry) or immersed in deuterated methanol and water: a) As-spun membranes; b) membranes exposed to MeOH vapor phase. The curves have been off-set arbitrarily to highlight their q -dependence; the -4 slope corresponds to Porod behavior (flat surface); c) Laboratory WAXD measurements from the as-spun and MeOH vapor-treated fiber mats.

Fig. 3 shows average Raman spectra from the electrospun silk fibroin membranes, before and after exposure to MeOH vapor (see Fig. S1 for the full collection of spectra). Each spectrum acquisition was preceded by 120 s laser illumination for fluorescence quenching. The residual fluorescence was responsible for baseline variations between same sample spectra, but their Raman features were very similar (Fig. S1). Even with no selection of the scattered polarization, just because the laser excitation is polarized, the intensity of each Raman band should depend on the orientation of non-isotropic samples. We did not notice intensity ratio variations from one point of analysis to the other (Fig. S1), including for the Amide I to Amide III ratio that is commonly used as an orientation marker [35] but this does not necessarily indicate the electrospun fibers are totally isotropic (our $\sim 5 \mu\text{m}^2$ laser spot probed several randomly oriented fiber segments at once).

It was observed that the exposure of the silk fibroin membranes to

MeOH vapor for 3 h has virtually no effect in the protein secondary structures (Fig. 3b). In order to quantify the structural rearrangement we applied a fitting procedure inspired by those from Maiti et al. [36] and Lefèvre et al. [35,37]: we used 4 Pseudo-Voigt profiles (with no bandwidth limit) to model contributions at 1635 cm^{-1} (unordered chains), 1653 cm^{-1} (helices), 1668 cm^{-1} (β -sheets) and 1682 cm^{-1} (unordered β turns). The results are shown in Fig. 3c and d. The latter confirms the limited effect of MeOH vapor on the secondary structure whereas the number of β -sheets found in a pristine cocoon fiber was near 60%. Note that we fitted the “pseudo-isotropic” cocoon spectrum from Lefèvre et al. [35,37] (a combination of polarized Raman spectra for which band areas are proportional to the actual proportion of the corresponding secondary structures) and found reasonable agreement with their results.

2.2. Nanoscale assessment of ferroelectric and piezoelectric properties of silk fibroin

The effect of the methanol treatment on the protein electroactive response was further explored by local piezoelectric response microscopy (PFM) of individual electrospun silk fibers. The AFM scanning shows that the electrospun fibers have a diameter of 200 nm (Fig. 4a and b) and their height is between 70 – 80 nm (Fig. 4c).

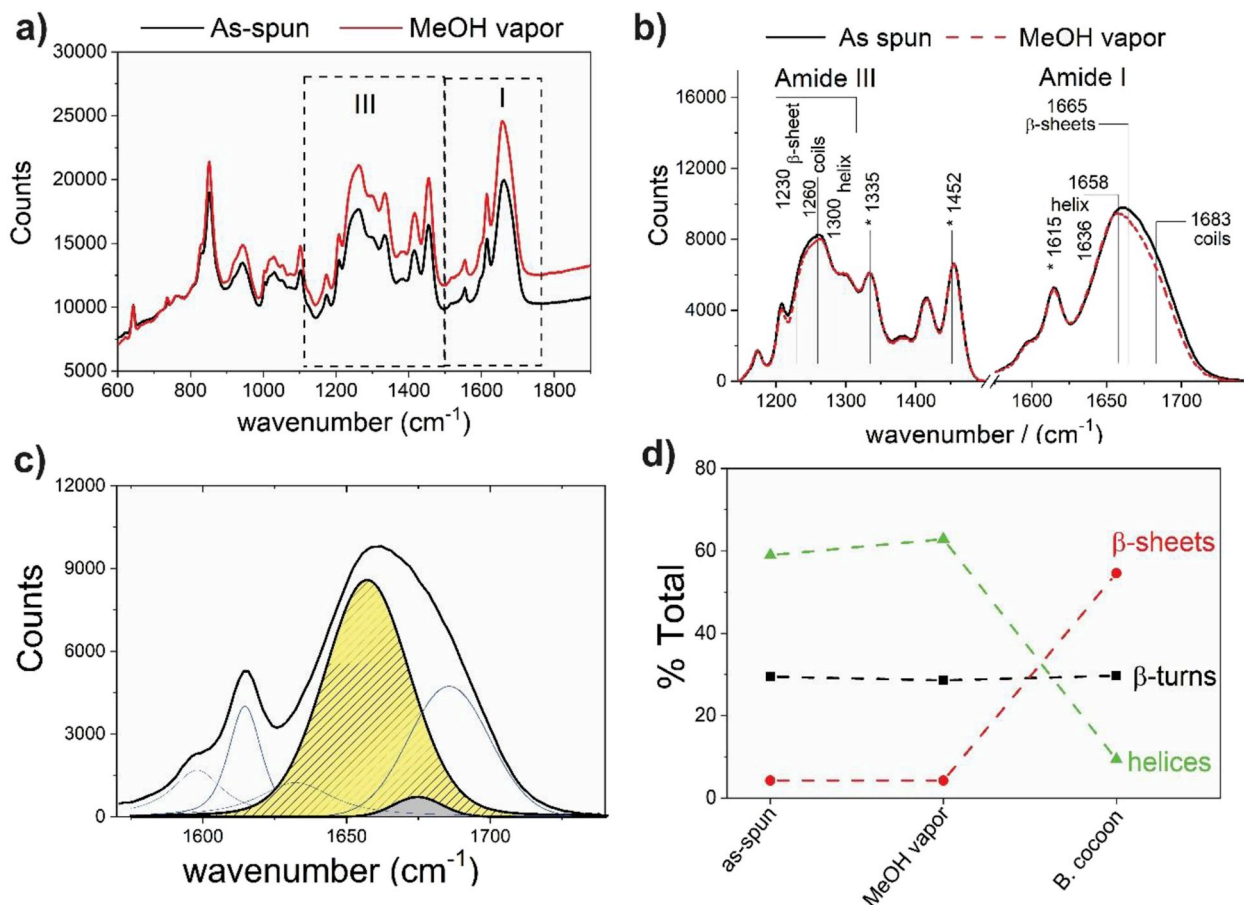


Fig. 3. a) Average of 300s Raman spectra for silk membranes probed before (“as-spun”; 18 measurements) and after 3hr-exposure to MeOH vapor (16 measurements) or submitted to MeOH vapor (18 measurements). Each acquisition was delayed by 120s for fluorescence quenching (see Fig. S1 inset). The dotted boxes indicate the spectral regions considered in Fig. 3b; b) The “as-spun” and “MeOH vapor” spectra from Fig. 3a after subtraction of linear segments attached to the curves at 1145, 1500 and 1750 cm^{-1} . The starred peaks correspond to scissoring modes (δ_{CH_3} @ 1335 cm^{-1} ; δ_{CH_2} @ 1452 cm^{-1}) and tyrosine/phenylalanine residues (1615 cm^{-1}); c) Spectral decompositions of the Amide I band for the as-spun membrane. The streaked yellow band corresponds to α -helices whereas the gray band is associated with β -sheets; d) The Raman-derived secondary structure distribution. The Bombyx cocoon data were obtained by our own fitting of a pseudo-isotropic spectrum from Ref. [38] (see text).

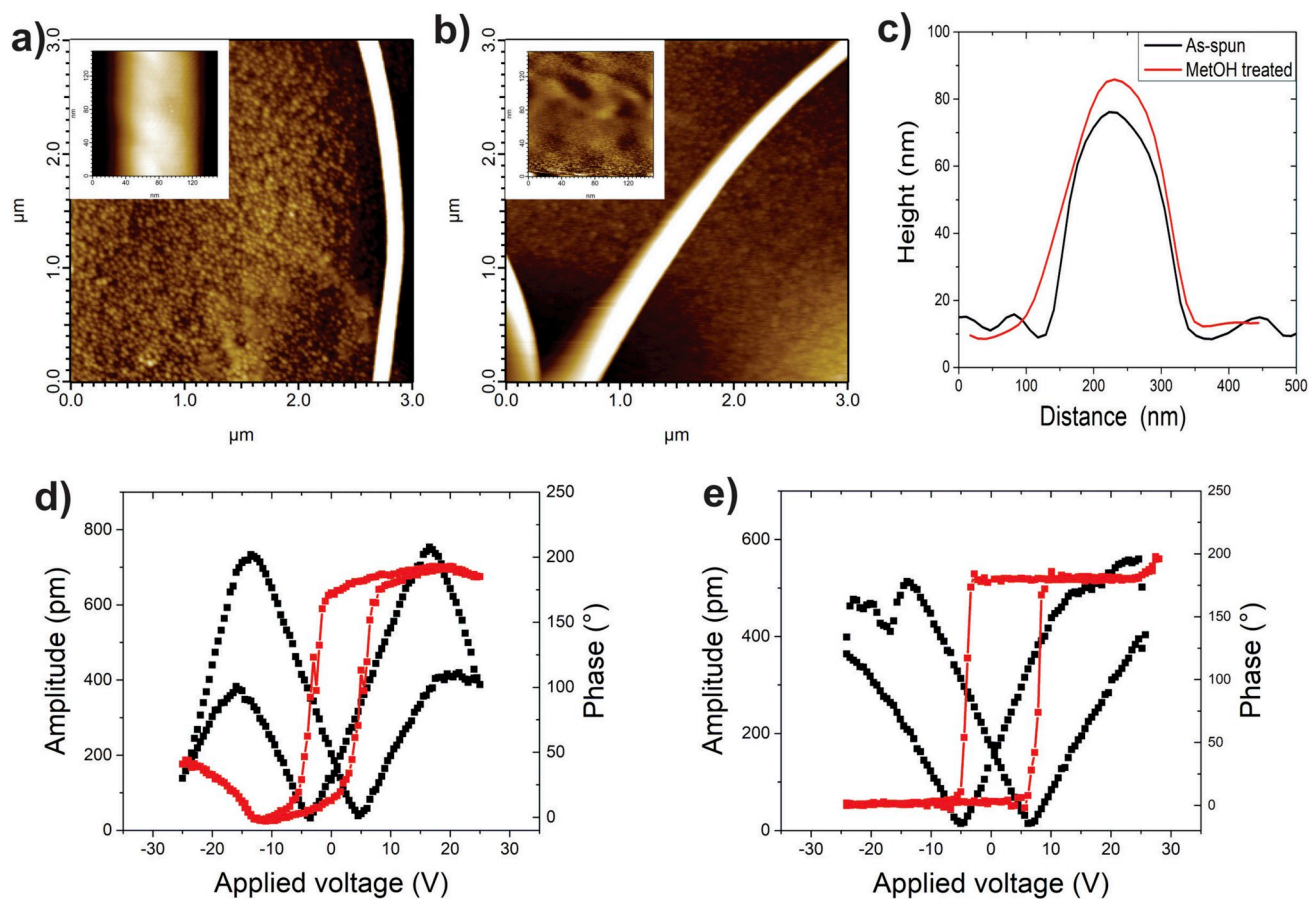


Fig. 4. Silk fibroin samples AFM topography: a) As-spun; b) Fiber treated with MeOH vapor phase; c) Height profile of the silk fibroin samples; d-e) PFM phase-voltage (red color) and amplitude-voltage (black color) for the as-spun sample and the fiber treated with MeOH vapor for 3 h.

A ferroelectric material will expand or contract under the presence of an applied electric field. In this work, voltage sweeps from -25 up to $+25$ V were applied to the conductive cantilever and the phase and amplitude responses recorded (Fig. 4d and e).

PFM results show that the as-spun and MeOH treated fibers have similar behaviors: their phase and amplitude vs. voltage curves show the rectangular and “butterfly loop” shapes that are characteristic of ferroelectric materials (Fig. 4d and e).

The butterfly loops are almost perfect, showing a good dipole reversibility when the applied field changes from positive to negative, and vice-versa. For the as-spun sample however, the amplitude goes up to a maximum and starts decreasing past a certain voltage (Fig. 4d). This behavior is due to the processing of the samples that stretches the droplet and drags the polymer chains in the longitudinal direction, due to the columbic forces in the jet [30]. This has the effect of reducing the fiber diameter and encourages a faster solvent evaporation, leading to a structure formed by small and/or fragmented crystallites. It was reported that a heterogeneous distribution of defects or composition inside a ferroelectric polymer leads to the formation of a double hysteresis loop when compared to a homogeneous composition polymer [39]. Furthermore, PFM experiments showed that when the electrospun sample is submitted to the MeOH vapor, the polymer chains start to redirect and organize in a more regular fashion, leading to a regular butterfly loop with a perfect rectangular hysteresis in the phase vs applied voltage diagram (Fig. 4e).

Based on the crystalline unit of silk fibroin, Fukada suggested that this protein could have a high piezoelectric constant [9]. Each point of

the “butterfly loop” carries information about the piezoelectric deformation ($\varepsilon_p = d_{ij}E_i$, where d_{ij} is the apparent piezoelectric constant and E is the applied electric field) and the apparent piezoelectric coefficient can be estimated from the slope of the amplitude vs voltage loop. We obtain a value of 38 ± 2 p.m./V for the as-spun fibers (28 ± 3 p.m./V for the sample submitted to MeOH vapor), which is 20-fold higher than the value reported for spider silk [40]. The values found in this work are also higher than those found for gelatin fibrous mats submitted to crosslinking with glutaraldehyde vapors [27] or collagen fibrils [41].

The longitudinal piezoelectric voltage coefficient $g_{33} = \frac{d_{33}}{\varepsilon_0 \varepsilon_r}$ (where d_{33} is the longitudinal piezoelectric charge coefficient, ε_0 is the vacuum permittivity and the electrospun silk fibroin dielectric constant, Fig. S4) was obtained from the hysteresis loops (Fig. 4d and e). The values found for the as-spun and methanol treated silk fibroin electrospun fibers were 1.05 and 0.53 Vm.N $^{-1}$, respectively. This shows that silk fibroin has a significantly higher electroactivity than PVDF (with a reported g_{33} of 0.287 Vm.N $^{-1}$) [42], PMN-PT single crystals ($g_{33} = 0.031$ Vm.N $^{-1}$) [43], and more traditional electroactive ceramics such as lead zirconate titanate (PZT, $g_{33} = 0.020$ to 0.026 Vm.N $^{-1}$) [17] and barium titanate (BaTiO $_3$, $g_{33} = 0.013$ Vm.N $^{-1}$) [16].

Piezoelectricity is not exclusively found in crystalline materials like PZT, but it can also be found in fully amorphous polymers like polyacrylonitrile, polyvinyl chloride, or polyphenylethnitrile [44]. The electroactive properties of amorphous polymers are due to the packing and configuration of the polar molecules, which determine the balance between the attractive and repulsive forces, ultimately influencing the

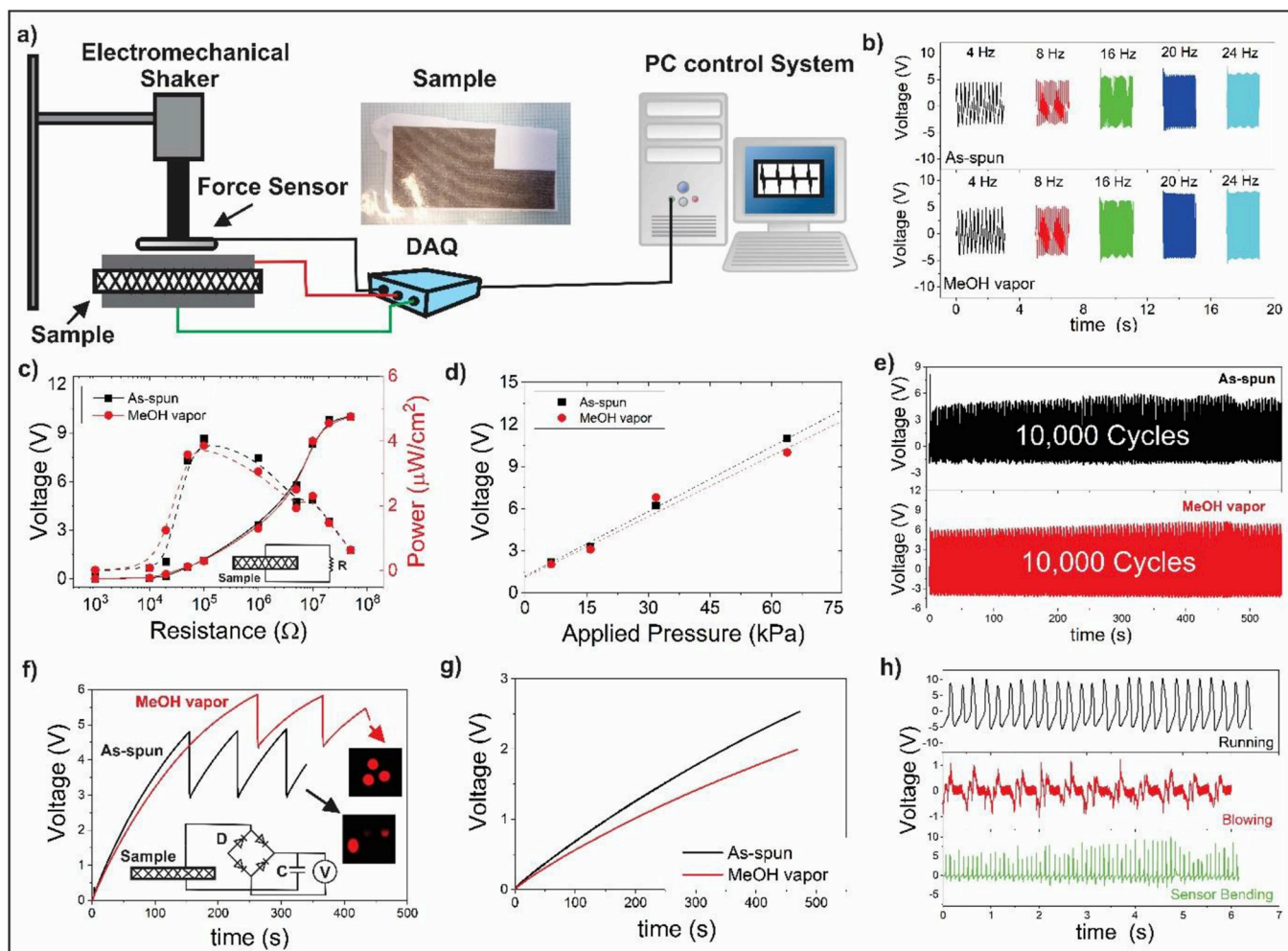


Fig. 5. a) Schematic of the setup used to measure the sensor piezoelectric performance; b) Generated voltage recorded with an applied pressure of 10 N oscillating at different frequencies; c) Variation of the voltage output and power density with resistance load (under a 32 kPa stress and a frequency of 4 Hz); d) Output voltage under different applied pressures; e) Stability test for silk fibroin samples before and after methanol vapor exposure, under a 32 kPa stress (16 Hz): the open circuit voltage was recorded as a function of time over 10,000 cycles; f) Charging voltage across a single $4.7 \mu\text{F}$ capacitor charged by the single nano-harvesters; the LEDs show the light emitted on discharge; g) Charging voltage across a single $10 \mu\text{F}$ capacitor charged by the individual nano-harvesters under a 32 kPa stress (16 Hz and h) The output voltage generated from the nano-harvesters subjected to bending, blowing, or glued on top of the insole of a walking man.

dipole-dipole interaction and orientation [45].

In silk fibroin α -helix and β -sheet regions, the C–O–N–H dipoles are preferentially oriented in the longitudinal direction of the fiber axis [19,20]. When the sample is pressed in the thickness direction, each individual dipole is slightly rotated in the helix direction or slightly displaced in the trans-planar zigzag conformation of the β -sheet. Finally, the sum of all these dipolar movements results in an electric polarization in the direction normal to the longitudinal axis of the fiber [19,20].

The unique combination of a high electrical field and the fast evaporation of the solvent during electrospinning produces a metastable state of highly aligned polymer chains inside the individual fiber, resulting in a high alignment of the C–O–N–H dipoles in the direction of the electric field, which leads to the outstanding piezoelectric and ferroelectric properties observed for the electrospun silk fibroin, making it an ideal candidate for self-powered e-skin sensors and nano energy harvesters.

2.3. Macroscopic assessment of silk fibroin piezoelectricity

Silk fibroin piezoelectricity was assessed at the macroscale by measurements of the energy harvested by the SF membranes under an oscillatory pressure. Silver electrodes were placed on both sides of the

membrane and the applied force was controlled by placing a force sensor on the shaking system that presses the sample (Fig. 5a). The frequency of the applied force does not play a significant role in the voltage output (Fig. 5b), and silk fibroin electrospun membranes showed an outstanding response time (τ_r) of 3 ms (supplementary information, Fig. S5), five times faster than the τ_r reported for gelatin electrospun fibers [27].

Previously reported triboelectric nanogenerators [46,47] and resistive sensors [48] had a high frequency limit of 10 and 4 Hz, respectively. The nanogenerators based on electrospun silk fibroin show better dynamic characteristics and could be useful for applications in harsh environments.

As-spun SF membranes and the SF sample submitted to methanol vapor showed a similar behavior and a maximum of 8 V was recorded for a frequency of 24 Hz (Fig. 5b). The dipole reversibility was assessed by reversing the electrode connections under the same imparting pressure and comparing the signals obtained from both measurements. The obtained results showed that there is dipole reversibility (Fig. S4) and prove the macroscopic piezoelectric character of the SF protein, already assessed at the nanoscale by PFM (Fig. 4).

The output power performance of the silk fibroin samples before and after MeOH treatment was assessed by connecting the nanogenerator with loads of different resistance (R_L), ranging from 1 k Ω to

Table 1

Comparison of SF electrical and piezoelectric properties against other electro-active materials.

Material	ϵ (1 kHz)	d_{33} (pm.N ⁻¹)	g_{33} (Vm.N ⁻¹)	Reference
Quartz	4.6	2	0.02	[55,56]
PZT-4	1400	-123	0.03	[57]
BaTiO ₃	1500	145	0.01	[57,58]
PVDF	12	-30	0.33	[57]
As-spun Silk fibroin	3.7	38	1.05	This work
Vapor MeOH Silk fibroin	6.0	27	0.53	This work

70 M Ω (under a frequency of 4 Hz). It was observed that the instantaneous voltage drop (V_L) across the resistors increases with the increment of R_L and a maximum V_L was recorded for a resistance of 100 k Ω , with a similar behavior as the open circuit. Continuing to increase R_L led to a decrease of the voltage output (Fig. 5c).

The output power density was calculated through $P = \frac{1}{A} \frac{V_L^2}{R_L}$, where A is the active area of the sensor. A maximum output power of 5 μ W cm⁻² was recorded for the silk fibroin nanogenerator (Fig. 5c) and could be potentially useful in wearable smart electronics and self-powered devices.

The voltage output (open circuit, V_{oc}) of the SF nanogenerators increases linearly with the applied mechanical pressure (σ_a , Fig. 5d). The sensibility (S) of the silk fibroin nanogenerators, defined as $S = \frac{\Delta V_{oc}}{\Delta \sigma_a}$, revealed that the SF energy harvesters had a value of 0.15 V kPa⁻¹, and the MeOH treatment didn't affect the material's performance. Moreover, the energy nanogenerator showed an outstanding operational stability

of $V_{oc} \sim 8$ V over 10,000 cycles (Fig. 5e).

The generated power can be stored into a battery or a capacitor after rectification of the alternating signal. A full-wave four probe bridge rectifier circuit was used under the cyclic applied force of 10 N and at a frequency of 16 Hz, and the energy generated by the nanogenerator was stored in a 4.7 μ F capacitor. The characteristic stepwise charge and discharge of the capacitor recorded for the samples before and after MeOH treatment in vapor phase is shown in Fig. 5f, and a voltage higher than 5 V was easily recorded after 140 s, which is remarkable when compared with other piezoelectric energy harvesters tested with a similar procedure [27,40,49–51].

The stepwise cyclic charge and discharge of the capacitor was performed to evaluate the stability of the SF harvester device, and it demonstrated that it was feasible to charge the capacitor and turn on several LEDs at multiple times (Fig. 5f), showing that silk fibroin is a promising candidate to scavenging energy from mechanical vibrations and power small low-power consumption electronic devices.

The charging performance of different capacitors (10 and 4.7 μ F) was tested under cyclic mechanical loading (10 N and 16 Hz) and it was observed that the voltage increases monotonously, as shown in Fig. 5g. The charge capacity of the silk fibroin electrospun membranes can be calculated through $E_{stored} = \frac{CV^2}{2}$, where C is the capacitance of the capacitor and V is the charging voltage across the capacitor at definite time t . Silk fibroin electrospun membranes can store energy up to 85 μ J, which is twice the amount reported for PVDF-AlO-rGO piezoelectric harvesters [50], or more than 3-fold the energy storage reported for the nanogenerator built from spider silk [40]. The amount of energy that the electrospun silk fibroin can generate and store is outstanding when

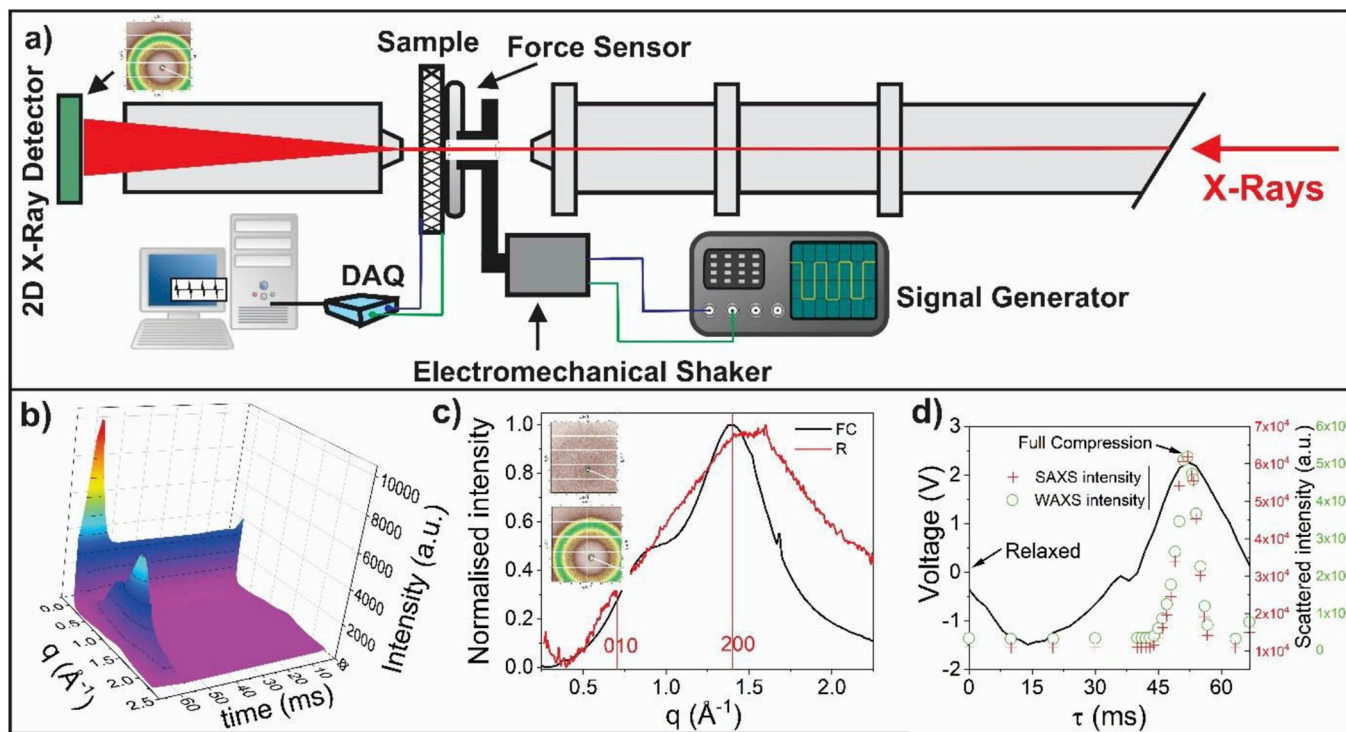


Fig. 6. a) Schematic (not to scale) of the synchrotron setup used for acquiring the SAXS signal, and the in-situ measurement of the sample voltage output during a mechanical excitation of 10 N at 15 Hz; b) Radial scattering profiles as function of time from the initiation of the sample compression (τ); c) 2D scattering patterns: the top pattern is from the sample during the initiation of the piezoelectric stimulus (FC label); and the bottom pattern is from relaxing signal (R label). The main panel shows the 1D radial scattering profiles from each 2D pattern. The two vertical red lines are indicative of two silk II lattice spacings together with hkl indices from Shen et al. [59]; and d) The black line shows the variation of voltage with applied mechanical stimulus (piezoelectric effect) during the variation of the time base τ . The scattered intensity at $q = 1.40 \text{ \AA}^{-1}$ (green circles) and the integral small angle intensity ($0.06 \text{ \AA}^{-1} < q < 0.20 \text{ \AA}^{-1}$) - red crosses) are plotted on the same time base.

Table 2
WAXD peak positions, characteristic spacings and features.

q_{\max} (\AA^{-1})	d (\AA)	Comments
Relaxed sample		
0.702	8.95	Very broad 010 [59]
1.403	4.48	Very broad 020 [59]
1.520	4.13	Very broad and weak
Fully compressed		
0.120	52.5	Sharp peak
0.383	16.41	Weak and broad
0.894	7.02	Broad
1.390	4.521	Broad
1.520	4.134	Weak and broad
1.684	3.732	Sharp and weak

compared to other nanocomposite harvesters based on PVDF [24,51–53], a well-established synthetic piezoelectric polymer.

The piezoelectric energy conversion efficiency (η) of the developed nano-harvesters was estimated as the ratio between the generated output electrical energy (E_{out}) and the applied mechanical energy (E_{in}). An efficiency of 18 and 21% was obtained for the as-spun and vapor treated silk fibroin membranes, respectively. Literature reports a wide range of η values; from 0.3% for the fish bladder [54], up to 66% for the spider silk [40]. However, η is strongly affected by the sample mechanical properties and thickness, and these could be the reason for the discrepant values reported in literature.

The energy generated by the silk fibroin electrospun harvester can be used to power up light emitting diodes (LEDs, Fig. 5f). With proper design, SF could thus be applied to generate and supply energy to power up several portable electronic devices, e.g. a watch or health wristband. Moreover, the human body is constantly generating movement like walking, jogging, bending, finger typing, breathing, heart beating, among many other oscillatory movements. These are potential biomechanical sources for energy scavenging from piezoelectric devices. In this work, the viability of the fabricated sensors as energy harvesters from biomechanical sources was explored not only to provide energy to self-powered electronic devices but also to monitor the human motion. The silk fibroin energy harvesters were submitted to bending, blowing and running solicitations (Fig. 5h).

The nano-harvester was capable to monitor the bending of the sensor during the movement of air against its surface and the pressure generated while running. Moreover, the running movement generated the highest voltage output when compared to the other conditions, which is due to the amount of pressure applied to the sensor. Overall, the silk fibroin presents unique piezoelectric properties, that must be further explored for human motion monitoring and wearable devices.

A complete overview of the electric and electroactive properties characterized in this study, and their comparison to other known piezoelectric materials is given in Table 1.

2.4. In-situ WAXD measurement during mechanical solicitation

WAXD has been used to monitor crystalline molecular packing in response to the same cyclic deformation that was responsible for the piezoelectric effect (Fig. 6a). Fig. 6b indicates the variation of the azimuthally averaged scattering patterns within the cycle of deformation. The patterns with the lowest and highest scattered intensities as well as the corresponding radial profiles are shown in Fig. 6c. The highest intensity pattern corresponds to the initiation of the mechanical stimulus (Full Compression – FC), and the lowest intensity pattern to relaxation back to equilibrium (relaxation – R). Both patterns, like the laboratory WAXD measurements, exhibit radial symmetry indicating no preferential orientation of structures. This is not surprising given the direction of measurement on membranes consisting of isotropically

oriented fibers; and the parallel nature of the mechanical stress and the transmission WAXD measurement. For further analysis we will concentrate on the radial profiles.

The 1-D profile designated FC, has one broad feature, which is in the same reciprocal space position as the 020 silk II lattice observed by Shen et al. [59]. Assignment of the silk II lattice is consistent with previously discussed Raman observations (Fig. 3). The peak shape is not symmetric which is indicative of other poorly defined underlying crystallographic features, and possibly the presence of a broad amorphous halo. In common with other fibrous biopolymers it is exceptionally difficult to reliably deconvolve the effects of lattice strain, crystallinity and crystallite size on the radial profile to extract structural information [60]. The radial profile from the FC membrane has the same peak as the silk II from sample R as well as a number extra of peaks, and a larger diffuse signal in the small angle domain. Table 2 tabulates the reciprocal space position and corresponding spacing's of these features. The peak labelled 200 in the silk II lattice does not vary in position in q -space and the intensity increases and decreases in phase with the deformation cycle (Fig. 6d).

A detailed crystallographic reconstruction of the changes in molecular packing which are responsible for the piezoelectric effect is beyond the information content (number of peaks) of these measurements. However, the above observations may be used to draw some general conclusions on the nature of the reversible restructuring during compressions. The growth of intensity in the diffracting species is not through the growth of existing crystalline domains (increasing coherence length), which would lead to a narrowing in line shapes, but rather reflects the formation of more domains with similar coherence length. The formation of more domains, or crystallites, is consistent with the parallel growth in the small angle scattering signal ($0.07 \text{\AA}^{-1} < q < 0.2 \text{\AA}^{-1}$) due to scattering off small grain boundaries.

3. Conclusions

In summary, the origin of the piezoelectric properties of silk fibroin, from the individual electrospun fibers to large-scale polymer membranes, was investigated. SF demonstrated a high apparent piezoelectric coefficient and maintained its good electroactive properties when the membranes were stabilized with methanol vapor. The methanol in the vapor phase limits the silk I to silk II phase transformation, preserving at some extent the dipole alignment, and the piezoelectric macroscopic assessment showed that the nano-harvesters can generate up to 8 V in open circuit. They also have a power density of $5 \mu\text{W}/\text{cm}^2$, with an outstanding dynamic pressure sensibility of 0.15 V/kPa, along with a high energy conversion efficiency (up to $\approx 21\%$). Their performance stability under mechanical cycling offers unique capability to power low power electronic devices and monitor different human movements.

Moreover, it was demonstrated that the outstanding electroactive properties of silk fibroin are due to the high alignment of the polymer chains and dipole orientation inside the fibers, leading to a high dipolar moment. This work represents a new insight into the origin of the piezoelectric properties of SF and opens new opportunities for applications in self-powered epidermal electronics, implantable medical devices, and personalized health care.

Acknowledgments

This research was undertaken on the Small/wide-angle X-ray scattering beamline at the Australian Synchrotron under the proposal numbers M12973 and M13374. The authors are thankful to Prof. Eiichi Fukada for his comments and discussions.

Appendix A. Supplementary data

Supplementary data to this article can be found online at <https://doi.org/10.1016/j.nanoen.2019.104106>.

References

- [1] T.D. Sutherland, J.H. Young, S. Weisman, C.Y. Hayashi, D.J. Merritt, Insect silk: one name, many materials, *Annu. Rev. Entomol.* 55 (1) (2010) 171–188.
- [2] J.L. Yarger, B.R. Cherry, A. van der Vaart, Uncovering the structure–function relationship in spider silk, *Nat. Rev. Mater.* 3 (2018) 18008.
- [3] S. Ling, D.L. Kaplan, M.J. Buehler, Nanofibrils in nature and materials engineering, *Nat. Rev. Mater.* 3 (2018) 18016.
- [4] S. Jokisch, M. Neuenfeldt, T. Scheibel, Silk-based fine dust filters for air filtration, *Adv. Sustain. Sys.* 1 (10) (2017) 1700079.
- [5] T. Yucel, M.L. Lovett, D.L. Kaplan, Silk-based biomaterials for sustained drug delivery, *J. Control. Release* 190 (2014) 381–397.
- [6] P. Bhattacharjee, B. Kundu, D. Naskar, H.-W. Kim, T.K. Maiti, D. Bhattacharya, S.C. Kundu, Silk scaffolds in bone tissue engineering: an overview, *Acta Biomater.* 63 (2017) 1–17.
- [7] D.N. Rockwood, R.C. Preda, T. Yücel, X. Wang, M.L. Lovett, D.L. Kaplan, Materials fabrication from *Bombyx mori* silk fibroin, *Nat. Protoc.* 6 (2011) 1612.
- [8] P. Aramwit, S. Kanokpanont, T. Nakpheng, T. Srichana, The effect of sericin from various extraction methods on cell viability and collagen production, *Int. J. Mol. Sci.* 11 (5) (2010) 2200.
- [9] E. Fukada, On the piezoelectric effect of silk fibers, *J. Phys. Soc. Jpn.* 11 (12) (1956) 1301A–1301A.
- [10] T. Yucel, P. Cebe, D.L. Kaplan, Structural origins of silk piezoelectricity, *Adv. Funct. Mater.* 21 (4) (2011) 779–785.
- [11] S. Inoue, K. Tanaka, F. Arisaka, S. Kimura, K. Ohtomo, S. Mizuno, Silk fibroin of *Bombyx mori* is secreted, assembling a high molecular mass elementary unit consisting of H-chain, L-chain, and P25, with a 6:6:1 molar ratio, *J. Biol. Chem.* 275 (51) (2000) 40517–40528.
- [12] K. Tanaka, S. Inoue, S. Mizuno, Hydrophobic interaction of P25, containing Asn-linked oligosaccharide chains, with the H-L complex of silk fibroin produced by *Bombyx mori*, *Insect Biochem. Mol. Biol.* 29 (3) (1999) 269–276.
- [13] A. Matsumoto, J. Chen, A.L. Collette, U.-J. Kim, G.H. Altman, P. Cebe, D.L. Kaplan, Mechanisms of silk fibroin Sol–Gel transitions, *J. Phys. Chem. B* 110 (43) (2006) 21630–21638.
- [14] B. Lotz, F. Colonna Cesari, The chemical structure and the crystalline structures of *Bombyx mori* silk fibroin, *Biochimie* 61 (2) (1979) 205–214.
- [15] J.-C. Dubois, Hari Singh Nalwa (Ed.), *Ferroelectric Polymers: Chemistry, Physics, and Applications*, vol. XII, Marcel Dekker, New York, 1995895 pp., hardcover, \$225.00, ISBN 0-8247-9468-0, *Advanced Materials* 8(6) (1996) 542–542.
- [16] K. Uchino, *Ferroelectric Devices*, second ed., CRC Press, 2009.
- [17] Yongke Yan, Kyung-Hoon Cho, Deepam Maurya, Amit Kumar, Sergei Kalinin, Armen Khachatryan, S. Priya, Giant energy density in [001]-textured Pb(Mg_{1/3}Nb_{2/3})O₃-PbZrO₃-PbTiO₃ piezoelectric ceramics, *Appl. Phys. Lett.* 102 (4) (2013) 042903.
- [18] S. Yun, Y. Zhang, Q. Xu, J. Liu, Y. Qin, Recent advance in new-generation integrated devices for energy harvesting and storage, *Nano Energy* 60 (2019) 600–619.
- [19] E. Fukada, Piezoelectricity of biopolymers, *Biorheology* 32 (6) (1995) 593–609.
- [20] E. Fukada, Piezoelectric properties of organic polymers, *Ann. N. Y. Acad. Sci.* 238 (1) (1974) 7–25.
- [21] V. Sencadas, C. Ribeiro, I.K. Bdiqin, A.L. Kholkin, S. Lanceros-Mendez, Local piezoelectric response of single poly(vinylidene fluoride) electrospun fibers, *Phys. Status Solidi (A) Appl. Mater. Sci.* 209 (12) (2012) 2605–2609.
- [22] J. Yan, M. Liu, Y.G. Jeong, W. Kang, L. Li, Y. Zhao, N. Deng, B. Cheng, G. Yang, Performance enhancements in poly(vinylidene fluoride)-based piezoelectric nanogenerators for efficient energy harvesting, *Nano Energy* 56 (2019) 662–692.
- [23] R.A. Surmenev, T. Orlova, R.V. Chernozem, A.A. Ivanova, A. Bartasyte, S. Mathur, M.A. Surmeneva, Hybrid lead-free polymer-based nanocomposites with improved piezoelectric response for biomedical energy-harvesting applications: a review, *Nano Energy* 62 (2019) 475–506.
- [24] J. Nunes-Pereira, V. Sencadas, V. Correia, V.F. Cardoso, W. Han, J.G. Rocha, S. Lanceros-Mendez, Energy harvesting performance of BaTiO₃/poly(vinylidene fluoride-trifluoroethylene) spin coated nanocomposites, *Compos. B Eng.* 72 (2015) 130–136.
- [25] Y. Cho, J.B. Park, B.-S. Kim, J. Lee, W.-K. Hong, I.-K. Park, J.E. Jang, J.I. Sohn, S. Cha, J.M. Kim, Enhanced energy harvesting based on surface morphology engineering of P(VDF-TrFE) film, *Nano Energy* 16 (2015) 524–532.
- [26] F. Eichi, Y. Iwao, Piezoelectric effects in collagen, *Jpn. J. Appl. Phys.* 3 (2) (1964) 117.
- [27] S.K. Ghosh, P. Adhikary, S. Jana, A. Biswas, V. Sencadas, S.D. Gupta, B. Tudu, D. Mandal, Electrospun gelatin nanofiber based self-powered bio-e-skin for health care monitoring, *Nano Energy* 36 (2017) 166–175.
- [28] V. Sencadas, C. Ribeiro, A. Heredia, I.K. Bdiqin, A.L. Kholkin, S. Lanceros-Mendez, Local piezoelectric activity of single poly(L-lactic acid) (PLLA) microfibers, *Appl. Phys. Mater. Sci. Process* 109 (1) (2012) 51–55.
- [29] E.N. Harvey, The luminescence OF adhesive tape, *Science* 89 (2316) (1939) 460–461.
- [30] R. Seeram, L. Teik-cheng, F. Kazutoshi, *An Introduction to Electrospinning and Nanofibers*, World Scientific Publishing Company, 2005.
- [31] V. Sencadas, D.M. Correia, A. Areias, G. Botelho, A.M. Fonseca, I.C. Neves, J.L. Gomez Ribelles, S. Lanceros Mendez, Determination of the parameters affecting electrospun chitosan fiber size distribution and morphology, *Carbohydr. Polym.* 87 (2) (2012) 1295–1301.
- [32] W.S. Dubner, J.M. Schultz, G.D. Wignall, Estimation of incoherent backgrounds in SANS studies of polymers, *J. Appl. Crystallogr.* 23 (1990) 469–475.
- [33] O. Spalla, General theorems in small-angle scattering, in: P. Lindner, T. Zemb (Eds.), *Neutrons, X-Rays, and Light: Scattering Methods Applied to Soft Condensed Matter*, Elsevier, 2004, pp. 49–71.
- [34] J.N. Israelachvili, *Intermolecular and Surface Forces*, Academic Press, 2010.
- [35] T. Lefèvre, S. Boudreault, C. Cloutier, M. Pézolet, Diversity of molecular transformations involved in the formation of spider silks, *J. Mol. Biol.* 405 (1) (2011) 238–253.
- [36] N.C. Maiti, M.M. Apetri, M.G. Zagorski, P.R. Carey, V.E. Anderson, Raman spectroscopic characterization of secondary structure in natively unfolded proteins: α -synuclein, *J. Am. Chem. Soc.* 126 (2004) 2399–2408.
- [37] T. Lefèvre, M.E. Rousseau, M. Pézolet, Protein secondary structure and orientation in silk as revealed by Raman spectromicroscopy, *Biophys. J.* 92 (8) (2007) 2885–2895.
- [38] T. Lefèvre, M.-E. Rousseau, M. Pézolet, Orientation-insensitive spectra for Raman microspectroscopy, *Appl. Spectrosc.* 60 (8) (2006) 841–846.
- [39] L. Qi, W. Qing, Ferroelectric polymers and their energy-related applications, *Macromol. Chem. Phys.* 217 (11) (2016) 1228–1244.
- [40] S.K. Karan, S. Maiti, O. Kwon, S. Paria, A. Maitra, S.K. Si, Y. Kim, J.K. Kim, B.B. Khatua, Nature driven spider silk as high energy conversion efficient bio-piezoelectric nanogenerator, *Nano Energy* 49 (2018) 655–666.
- [41] D. Denning, J.I. Kilpatrick, E. Fukada, N. Zhang, S. Habelitz, A. Fertala, M.D. Gilchrist, Y. Zhang, S.A.M. Tofail, B.J. Rodriguez, Piezoelectric tensor of collagen fibrils determined at the nanoscale, *ACS Biomater. Sci. Eng.* 3 (6) (2017) 929–935.
- [42] M. Li, H.J. Wondergem, M.-J. Spijkman, K. Asadi, I. Katsouras, P.W.M. Blom, D.M. de Leeuw, Revisiting the δ -phase of poly(vinylidene fluoride) for solution-processed ferroelectric thin films, *Nat. Mater.* 12 (2013) 433.
- [43] Shujun Zhang, Sung-Min Lee, Dong-Ho Kim, Ho-Yong Lee, T.R. Shrout, Temperature dependence of the dielectric, piezoelectric, and elastic constants for Pb(Mg_{1/3}Nb_{2/3})O₃-PbZrO₃-PbTiO₃ piezocrystals, *J. Appl. Phys.* 102 (11) (2007) 114103.
- [44] Z. Ounaies, J.A. Young, J.S. Harrison, An overview of the piezoelectric phenomenon in amorphous polymers, field responsive polymers, *Am. Chem. Soc.* (1999) 88–103.
- [45] R.G.C. Arridge, C.G. Cannon, Calculation of the CONH dipole contribution to lattice energies of amides, polyamides, and polypeptides, *Proc. R. Soc. Lond. Ser. A Math. Phys. Sci.* 278 (1372) (1964) 91–109.
- [46] X.-S. Zhang, M.-D. Han, R.-X. Wang, F.-Y. Zhu, Z.-H. Li, W. Wang, H.-X. Zhang, Frequency-multiplication high-output triboelectric nanogenerator for sustainably powering biomedical microsystems, *Nano Lett.* 13 (3) (2013) 1168–1172.
- [47] T. Cheng, Y. Li, Y.-C. Wang, Q. Gao, T. Ma, Z.L. Wang, Triboelectric nanogenerator by integrating a cam and a movable frame for ambient mechanical energy harvesting, *Nano Energy* 60 (2019) 137–143.
- [48] S. Gong, W. Schwalb, Y. Wang, Y. Chen, Y. Tang, J. Si, B. Shirinzadeh, W. Cheng, A wearable and highly sensitive pressure sensor with ultrathin gold nanowires, *Nat. Commun.* 5 (2014) 3132.
- [49] A. Sultana, S.K. Ghosh, V. Sencadas, T. Zheng, M.J. Higgins, T.R. Middya, D. Mandal, Human skin interactive self-powered wearable piezoelectric bio-e-skin by electrospun poly-L-lactic acid nanofibers for non-invasive physiological signal monitoring, *J. Mater. Chem. B* 5 (35) (2017) 7352–7359.
- [50] S.K. Karan, R. Bera, S. Paria, A.K. Das, S. Maiti, A. Maitra, B.B. Khatua, An approach to design highly durable piezoelectric nanogenerator based on self-poled PVDF/AIO-rGO flexible nanocomposite with high power density and energy conversion efficiency, *Adv. Energy Mater.* 6 (20) (2016) 1601016.
- [51] A. Tamang, S.K. Ghosh, S. Garain, M.M. Alam, J. Haerberle, K. Henkel, D. Schmeisser, D. Mandal, DNA-assisted β -phase nucleation and alignment of molecular dipoles in PVDF film: a realization of self-poled bioinspired flexible polymer nanogenerator for portable electronic devices, *ACS Appl. Mater. Interfaces* 7 (30) (2015) 16143–16147.
- [52] J. Nunes-Pereira, V. Sencadas, V. Correia, J.G. Rocha, S. Lanceros-Mendez, Energy harvesting performance of piezoelectric electrospun polymer fibers and polymer/ceramic composites, *Sens. Actuators A Phys.* 196 (2013) 55–62.
- [53] S. Garain, T.K. Sinha, P. Adhikary, K. Henkel, S. Sen, S. Ram, C. Sinha, D. Schmeißer, D. Mandal, Self-poled transparent and flexible UV light-emitting cerium complex–PVDF composite: a high-performance nanogenerator, *ACS Appl. Mater. Interfaces* 7 (2) (2015) 1298–1307.
- [54] Sujoy Kumar Ghosh, D. Mandal, High-performance bio-piezoelectric nanogenerator made with fish scale, *Appl. Phys. Lett.* 109 (10) (2016) 103701.
- [55] V.E. Bottom, Dielectric constants of quartz, *J. Appl. Phys.* 43 (4) (1972) 1493–1495.
- [56] M.W. Hooker, Properties of PZT-based piezoelectric ceramics between-150 and 250° C, *Nat. Aeronaut. Space Administration* (1998) 1–25.
- [57] Z. Yang, S. Zhou, J. Zu, D. Inman, High-performance piezoelectric energy harvesters and their applications, *Joule* 2 (4) (2018) 642–697.
- [58] M. Acosta, N. Novak, V. Rojas, S. Patel, R. Vaish, J. Koruza, G.A. Rossetti, J. Rödel, BaTiO₃-based piezoelectrics: fundamentals, current status, and perspectives, *Appl. Phys. Rev.* 4 (4) (2017) 041305.
- [59] Y. Shen, M.A. Johnson, D.C. Martin, Microstructural characterization of *Bombyx mori* silk fibers, *Macromolecules* 31 (25) (1998) 8857–8864.
- [60] C.J. Garvey, I.H. Parker, G.P. Simon, On the interpretation of X-ray diffraction powder patterns in terms of the nanostructure of cellulose I fibres, *Macromol. Chem. Phys.* 206 (15) (2005) 1568–1575.



Vitor Sencadas is a Senior Lecture at University of Wollongong, and group leader of the Smart Macromolecules Research Group, Associate Investigator of the ARC Centre of Excellence for Electromaterials (ACES, Australia) and Associate Researcher of the Illawarra Health & Medical Research Institute (IHMRI). His work is focused in polymer based smart materials for stretchable sensors and actuators, energy harvesting and storage, biomedical and environmental applications.



Jacob Kirkensgaard received his PhD in Polymer Physics in 2010 at University of Copenhagen. He spent a number of years at the Niels Bohr Institute but has recently moved to Food Science to work on Structural Food Physics. His major research interests are centred around mesoscale self-assembly and particularly the formation of geometrically and topologically complex structures in soft matter systems, both synthetic systems and from various biological and food-based systems. He has combined expertise in coarse-grained molecular dynamics simulations of soft matter self-assembly and in structural investigations using x-ray and neutron scattering techniques.



Christopher Garvey uses advanced physical characterisations to understand the interface between materials science and biology. He holds a PhD from the Department of Chemical Engineering at Monash University and an MSc in Physical Chemistry from the University of Sydney. He is currently on secondment from the Australian Nuclear Science and Technology Organisation to a joint position between Lund and Malmö Universities.



Dr. Gwenaël Gouadec (born in 1973) received his Ph.D. degree in Physics from the University of Rennes I. In 2003, following a postdoctoral fellowship at the University of Alabama at Birmingham, he was appointed Assistant Professor at P. & M. Curie University (now Sorbonne-Université). A member of Monaris laboratory, he teaches physical chemistry and does research on solid state Raman spectroscopy (fiber- and CNT-reinforced composites, CdS and SiC crystallites, metallic nanoparticles, spider silk, directionally solidified eutectics, ...). His publishing record includes a reference Review paper (> 600 citations) and two book chapters on the Raman spectroscopy of nanomaterials.



Dr. Stephen Mudie is the senior scientist on the Australian Synchrotron Small and Wide Angle X-ray Scattering (SAXS/WAXS) Beamline, ANSTO. He received his Ph.D. in Physics from Monash University in 2005, and has worked on the SAXS/WAXS beamline since 2008. His work has focused on developing the beamline to a world class standard and supporting the many scientists using the facility. To date the beamline is acknowledged by more than 900 journal papers. His particular interest is software development for SAXS data reduction and experimental control and design.



Samuel Hauser received his Bachelor of Engineering in the field of Mechatronics at Reutlingen University in 2017. Currently he is studying on a master's programme and is expected to obtain a master's degree in the field of Mechatronics in 2019. During his time as a student he was able to complete several internships as well as a research semester, where his work was focused on algorithm development, physical modelling as well as sensor data processing. After finishing his master's degree, he will work for Bosch Sensortec GmbH as a software engineer.